ORIGINAL ARTICLE

JBMR

# Accuracy of High-Resolution In Vivo Micro Magnetic Resonance Imaging for Measurements of Microstructural and Mechanical Properties of Human Distal Tibial Bone

X Sherry Liu,[1]* X Henry Zhang,[2]* Chamith S Rajapakse,[3] Michael J Wald,[3] Jeremy Magland,[3] Kiranjit K Sekhon,[2] Mark F Adam,[4] Paul Sajda,[5] Felix W Wehrli,[3] and X Edward Guo[2]

[1]Division of Endocrinology, Department of Medicine, Columbia University, New York, NY, USA
[2]Bone Bioengineering Laboratory, Department of Biomedical Engineering, Columbia University, New York, NY, USA
[3]Department of Radiology, University of Pennsylvania, Philadelphia, PA, USA
[4]Department of Applied Physics and Applied Mathematics, Columbia University, New York, NY, USA
[5]Laboratory for Intelligent Imaging and Neural Computing, Department of Biomedical Engineering, Columbia University, New York, NY, USA

## ABSTRACT

Micro magnetic resonance imaging (μMRI) is an in vivo imaging method that permits 3D quantification of cortical and trabecular bone microstructure. μMR images can also be used for building microstructural finite element (μFE) models to assess bone stiffness, which highly correlates with bone's resistance to fractures. In order for μMRI-based microstructural and μFE analyses to become standard clinical tools for assessing bone quality, validation with a current gold standard, namely, high-resolution micro computed tomography (μCT), is required. Microstructural measurements of 25 human cadaveric distal tibias were performed for the registered μMR and μCT images, respectively. Next, whole bone stiffness, trabecular bone stiffness, and elastic moduli of cubic subvolumes of trabecular bone in both μMR and μCT images were determined by voxel-based μFE analysis. The bone volume fraction (BV/TV), trabecular number (Tb.N*), trabecular spacing (Tb.Sp*), cortical thickness (Ct.Th), and structure model index (SMI) based on μMRI showed strong correlations with μCT measurements ($r^2 = 0.67$ to 0.97), and bone surface-to-volume ratio (BS/BV), connectivity density (Conn.D), and degree of anisotropy (DA) had significant but moderate correlations ($r^2 = 0.33$ to 0.51). Each of these measurements also contributed to one or many of the μFE-predicted mechanical properties. However, model-independent trabecular thickness (Tb.Th*) based on μMRI had no correlation with the μCT measurement and did not contribute to any mechanical measurement. Furthermore, the whole bone and trabecular bone stiffness based on μMRI were highly correlated with those of μCT images ($r^2 = 0.86$ and 0.96), suggesting that μMRI-based μFE analyses can directly and accurately quantify whole bone mechanical competence. In contrast, the elastic moduli of the μMRI trabecular bone subvolume had significant but only moderate correlations with their gold standards ($r^2 = 0.40$ to 0.58). We conclude that most microstructural and mechanical properties of the distal tibia can be derived efficiently from μMR images and can provide additional information regarding bone quality. © 2010 American Society for Bone and Mineral Research.

**KEY WORDS:** BONE MICROSTRUCTURE; BONE STIFFNESS; FINITE ELEMENT MODEL; MICRO MAGNETIC RESONANCE IMAGING; MICRO COMPUTED TOMOGRAPHY

## Introduction

Osteoporosis, a metabolic bone disease of major proportions, is classically diagnosed by dual-energy X-ray absorptiometry (DXA) via areal bone mineral density (aBMD). It is becoming increasingly apparent, however, that other factors, independent of aBMD, contribute significantly to fracture risk.[1] Evidence for an independent role of bone microarchitecture as a determinant of the bone's mechanical competence and fracture risk has been documented in many studies.[2–8] Thus there has been great interest in developing new in vivo imaging methods capable of measuring bone microstructure that then could be used to derive new quantitative microstructural and mechanical measures for the clinical detection of osteoporosis. One such technology is micro magnetic resonance imaging (μMRI). MRI is an important focus for in vivo trabecular bone morphometry

Received in original form October 27, 2009; revised form February 15, 2010; accepted March 18, 2010. Published online March 26, 2010.
Address correspondence to: X Edward Guo, PhD, Department of Biomedical Engineering, Columbia University, 351 Engineering Terrace, Mail Code 8904, 1210 Amsterdam Avenue, New York, NY 10027, USA. E-mail: ed.guo@columbia.edu
*XS Liu and XH Zhang contributed equally to this work.

Journal of Bone and Mineral Research, Vol. 25, No. 9, September 2010, pp 2039–2050
DOI: 10.1002/jbmr.92

because of its absence of ionizing radiation, high innate contrast between bone and marrow, and widely distributed population of general-purpose clinical MRI instruments.[3,7–18] μMRI permits the visualization and quantification of trabecular network architecture at voxel sizes comparable with trabecular thickness, which makes the method sufficient for resolving individual microstructural elements and quantifying network topology. μMRI images can also be used for building microstructural finite element (μFE) models to assess bone stiffness,[6,18,19] a measurement which highly correlates with bone's resistance to fractures. Currently, the signal-to-noise ratio (SNR) of μMRI confines the scan to locations that permit the use of either a closely coupled volume transmit-receive coil or surface coil arrays, for example, the distal radius,[7,9,20] the distal tibia,[11,12] and the calcaneus,[3,8,15,21] in order to achieve a resolution close to the low end of trabecular thickness. Measurements of microstructure at the proximal femur also have been reported, albeit at a considerably lower resolution.[22] In several clinical studies, high-resolution in vivo μMRI has been performed at the distal radius, distal tibia, and calcaneus to assess trabecular bone microstructure. The morphological and mechanical properties of trabecular bone derived from in vivo μMRI have associations with fracture risk and are sensitive to drug interventions.[6,7,11,12,17,18,23,24]

A few in vitro validation studies have compared the microstructural measurements of high-resolution μMR images of trabecular bone samples from the distal radius and calcaneus with either micro computed tomography (μCT) or contact radiography and showed significant correlations.[14,20,25–27] μMRI image-based μFE predictions of trabecular bone samples have also been validated with μCT-based μFE predictions as standard reference.[28] However, these existing studies focused on the measurements of small bone samples or volumes of interest. Currently, there is no data validating μMRI of whole bone segments. Microstructural analyses of μMRI images of whole bone segments can provide more accurate estimates of trabecular bone microstructure as the inhomogeneity of the trabecular network can be taken into consideration, and additional measurement of cortical thickness can be provided. Moreover, whole bone stiffness can provide an estimate of the overall mechanical competence with the contributions from both the trabecular and cortical bone compartments. In order for μMRI-based microstructural and μFE analyses to become standard clinical tools for assessing bone quality, the data from μMRI must be thoroughly validated and compared with those from a current gold standard, namely, high-resolution μCT.

In this study, one of the primary purposes was to validate the 3D model-independent microstructural measurements of 1.5 T high-resolution μMRI against gold standard μCT measurements of the distal tibia. The second purpose was to validate the axial stiffness of the distal tibial bone segment, with and without the cortex, as assessed by μMRI-based μFE models against its gold standard, μCT-based μFE measurement. In addition, the anisotropic elastic moduli of trabecular bone based on μFE analyses of cubic subvolumes of μMR images were also compared with those of μCT images. Lastly, the ability of μMRI microstructural measurements to predict mechanical properties calculated by μCT-based μFE analyses was investigated. This represents the first validation study for μMRI-based microstructural and mechanical measurements of whole bone segments of human distal tibia.

## Materials and Methods

### Specimen preparation and μCT imaging

Twenty-five freshly frozen human cadaveric tibias from 15 donors (10 pairs and 5 singles, 11 males and 4 females) were obtained from the International Institute for the Advancement of Medicine (Scranton, PA, USA). The age of donors ranged from 55 to 84 years, with an average of 70.6 years. The donors' medical histories were screened to exclude metabolic bone diseases and chronic conditions that could affect bone metabolism, such as osteomalacia, Paget disease, primary hyperparathyroidism, chronic kidney disease, chronic obstructive pulmonary disease, HIV positivity, or bone cancer. However, donors could still have osteoporosis. Using a band saw, starting at approximately 15 mm proximal to the tibia endplate, each distal tibia was cut into a 25-mm section along the axial direction. The central 10-mm section along the axial direction was then scanned with a μCT system (vivaCT 40 or μCT 80, Scanco Medical AG, Bassersdorf, Switzerland). An ex vivo scanning setting (70 kVp, 114 μA, 700-ms integration time) was used for the μCT scanning, resulting in an isotropic 25-μm voxel size.

### μMRI

After μCT scanning, the bone marrow was removed from the distal tibial bone segments using a gentle water jet. Then each demarrowed bone segment was placed in a 250-mL cylindrical glass jar, immersed in 1 mM aqueous gadolinium–diethylene-triammine-pentaacetate (Gd-DTPA) to shorten the longitudinal relaxation time to that approximating fatty bone marrow ($T_1 \approx 300$ ms at 64 MHz). Each bone segment's anatomic orientation was aligned carefully with two distilled-water-filled capillary tubes attached to the inner surface of each jar, the large (small) capillary tube marking the anterior (medial) side of the specimen. Air bubbles trapped in the marrow spaces (which would cause artifactual signal voids and susceptibility artifacts) were removed through centrifugation at 1500 rpm (approximately 6*g*).[29] The specimens were imaged distal end first (analogous to feet first in patient scans) and anterior side up (analogous to supine position in patient scans) on a 1.5-T whole-body clinical MRI scanner (Siemens MAGNETOM Sonata, Siemens Medical Solutions, Erlangen, Germany) equipped with 40 mT/m gradients using an in-house-built receive-only two-element phased-array surface coil for imaging the ankle. Axial and sagittal localizer spin-echo images were acquired to prescribe the high-resolution 20-mm (inferosuperior) imaging slabs. The pulse sequence used was a more advanced and robust version of the 3D fast large-angle spin-echo (FLASE) pulse sequence[30] detailed in Magland and colleagues.[31] The center of this slab was selected as the center of the 25-mm bone segments. The FLASE pulse sequence used the following parameters: flip angle = 140 degrees; TR/TE = 80/10.5 ms; readout bandwidth = 7.81 kHz; field of view = 7 × 6.4 cm; 32 slices within the inferior-superior slab; 512 data points along the frequency-encoding direction

(anterior-posterior); and 460 phase-encoding points for the distal tibia. The typical acquisition time was 16 minutes and 23 seconds for the distal tibia, yielding a final raw data voxel size of $160 \times 160 \times 160\ \mu m^3$.

Next, the 3D grayscale images were input into the virtual bone biopsy (VBB) data-processing chain to yield thresholded binary images. Briefly, a local threshold algorithm was applied to correct marrow-intensity variations resulting from the sensitivity profile of the surface coil.[32] The images were then *sinc*-interpolated by a factor of $3 \times 3 \times 3$ by zero filling in the *k*-space domain resulting in, after Fourier transformation, a final image voxel size of $53 \times 53 \times 53\ \mu m^3$.[33] These images were then contrast inverted to yield a bone volume fraction (BVF) map in which voxel intensities ranged from 0 to 100 such that 0 was pure marrow and 100 represented pure bone. Here the images were thresholded at an empirically optimized value of 50% BVF to yield 3D binary images.[33] This thresholding procedure and setting are being used in the current μMRI clinical studies of human subjects.

## Mutual information–based registration of μMRI and μCT Images

To register the μCT images to μMR images, a pyramid three-step registration approach was employed using the landmark-initialized mutual information–based registration toolkit[34,35] of an open-source software (National Library of Medicine Insight Segmentation and Registration Toolkit, USA).[36] The subvoxel processed grayscale μMR images were held in fixed position while the grayscale μCT images were rotated and translated to match the μMR images. The registration accuracy was tested on simulated images and showed an alignment error smaller than 10% of the μCT voxel size (2.5 μm). All μCT images were registered successfully to the corresponding μMR images to encompass the same volume of interest (Fig. 1) and were confirmed by visual inspection using an open-source medical image display application (FusionViewer).[37]

## Standard 3D model-independent morphological analyses of μCT images

The standard μCT evaluation protocol was performed for the registered μCT images. First, the endosteal cortical surface was contoured semiautomatically to segment the trabecular and cortical regions, followed by Gaussian filtering and specimen-specific global thresholding to extract the mineralized phase using the standard protocol of Scanco software (Scanco Medical AG, Bassersdorf, Switzerland) for μCT analysis. Based on the thresholded trabecular bone images, the bone volume fraction (BV/TV) and 3D model-independent parameters trabecular thickness (Tb.Th*), trabecular spacing (Tb.Sp*), and trabecular number (Tb.N*) were determined based on a distance transformation.[38] In addition, the bone surface-to-volume ratio (BS/BV), structure model index (SMI), connectivity density (Conn.D), and degree of anisotropy (DA) were also evaluated for each trabecular bone image. BS/BV was computed by dividing the trabecular bone surface (BS) by the trabecular bone volume (BV), with BS and BV determined by a triangulation approach.[39] The SMI estimates, on average, the plate versus rod characteristics of trabecular bone.[40–43] For an ideal plate to an ideal rod structure, SMI ranges from 0 to 3, respectively. Conn.D quantifies trabecular connectivity by calculating the number of handles or closed loops in the trabecular network.[44,45] DA reflects the orientation of the trabecular bone network.[46,47] To evaluate the cortical thickness (Ct.Th), both periosteal and endosteal surfaces of the tibial cortex were contoured manually using the semiautomatic Scanco software to isolate the cortex as the volume of interest. The Ct.Th was determined as the cortical volume divided by the mean of the periosteal and endosteal bone surface areas according to a standard Scanco protocol for μCT images. All morphological analyses of the μCT images were performed using the standard morphologic analysis software on an HP AlphaStation of a VivaCT 40 system (Scanco Medical).

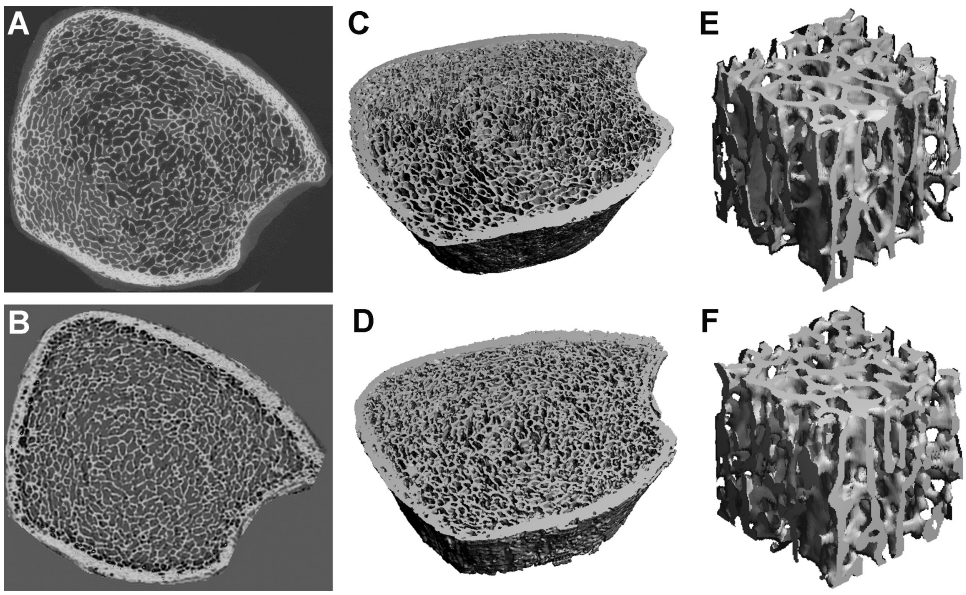


**Fig. 1.** The registered 2D grayscale images (*A*, *B*), 3D thresholded images (*C*, *D*), and 3D cubic subvolumes (*E*, *F*) of μCT and μMRI images of human distal tibia. The first row shows the high-resolution μCT images, and the second row shows the corresponding μMR images.

## Morphological analyses for μMR Images

All μMR images were analyzed by two evaluation protocols. First, the standard 3D model-independent morphological analyses were applied to the thresholded μMR images at a 53-μm voxel size. The BV/TV, Tb.N*, Tb.Th*, Tb.Sp*, Ct.Th, SMI, BS/BV, DA, and Conn.D values of each μMR image were calculated. The methods of these analyses are the same as the standard morphological analysis for μCT images, as described in the preceding section.

Due to the limited resolution of μMR images, a 2D analysis using the mean intercept length method based on the plate model has been used widely to achieve evaluation of trabecular bone microstructure.[14,26,48,49] This 2D analysis was applied to each μMR images to derive Tb.N, Tb.Th, and Tb.Sp. The same set of parameters derived by the 3D model-independent method was denoted by an asterisk (ie, Tb.N*, Tb.Th*, and Tb.Sp*) to distinguish them from the 2D parameters.

## Finite element analyses for μMR and μCT images

Three μFE analyses were performed for each μMR and μCT image. The first analysis was performed for the whole tibial bone segment to determine its axial stiffness. The second analysis was conducted for the tibial trabecular bone segment without the cortex to determine the trabecular bone axial stiffness. The third analysis was applied to a cubic subvolume of trabecular bone selected from the center of the sample to calculate the full anisotropic elastic moduli by using strict uniaxial strain boundary conditions.[50] These three μFE analyses provide distinct mechanical parameters of the distal tibia that are important in clinical assessments of mechanical competence. The axial stiffness is the overall mechanical competence, whereas trabecular bone axial stiffness provides an estimation of the overall structural contributions of the trabecular bone compartment. The subvolume trabecular bone μFE analysis reveals important anisotropic material properties of the trabecular bone component. Each bone voxel of a thresholded μMR image was converted directly to an 8-node elastic brick element with an element size of $53 \times 53 \times 53\,\mu m^3$. Each μCT image was resampled from 25 to 40 μm and then converted to μFE models with an element size of $40 \times 40 \times 40\,\mu m^3$. A convergence study was conducted in three randomly selected μCT images to determine the axial stiffness with different element sizes (25, 30, 40, 60, and 80 μm). Results showed that the maximum difference in axial stiffness between the models constructed at 40 and 25 μm was 1.67%. For each μFE analysis, bone tissue was modeled as an isotropic, linearly elastic material with a Young's modulus ($E_s$) of 15 GPa and a Poisson's ratio of 0.3 for all the models.[51] This assumption focuses the current study to imaging-related issues rather than variations in bone tissue properties, which currently cannot be assessed in patients. To evaluate axial stiffness for a whole bone segment with and without the cortical shell, a uniaxial displacement equaling 1% of the bone segment height was applied perpendicularly to the distal surface of the tibia while the proximal surface was imposed with zero displacement along the same direction. Both ends of the tibia were allowed to translate freely in the transverse plane. The total reaction force was calculated from the linear FE analysis, and the axial stiffness was calculated as the reaction force divided by the imposed displacement. The parallel FE program Olympus was used to solve these FE models.[52] Olympus is built on a serial finite-element analysis program (FEAP),[37] a parallel multigrid equation solver called Prometheus,[53] and the parallel numerical framework PETSc.[54] All the parallel computations were conducted on an IBM Power4 supercomputer (IBM Corporation, Armonk, NY, USA) at the San Diego Supercomputer Center using a maximum of 256 CPUs in parallel. Whole bone segment stiffness and trabecular bone stiffness were calculated for each μMR and μCT image, respectively.

A $143 \times 143 \times 143$ voxel cubic subvolume of trabecular bone was extracted from each registered and resampled μCT image (40-μm voxel size) corresponding to a $108 \times 108 \times 108$ voxel cubic subvolume (53-μm voxel size) from the μMR image (Fig. 1), which was equivalent to a physical size of $5.74 \times 5.74 \times 5.74\,mm^3$. The subvolumes from the two modalities were converted to μFE models. Using a customized element-by-element preconditioned conjugate gradient solver,[55] six μFE analyses were performed for each model, representing three strict uniaxial compressions along the three imaging axes (*x*, *y*, and *z*) and three strict uniaxial shears.[50] The general anisotropic stiffness matrix was first determined based on the results from the preceding analyses. A new coordinate system of orthotropic axes ($X_1$, $X_2$, and $X_3$) representing the best orthotropic symmetry was then calculated by using a numerical optimization algorithm, Powell's method,[56] to minimize an orthotropy objective function.[50] Transformation of the anisotropic matrix to a new coordinate system yielded the full orthotropic stiffness tensor.[50] The elastic constants and stiffness matrix were sorted such that $E_{11}$ was in the direction of the lowest axial modulus and $E_{33}$ was in the direction of the highest axial modulus. The elastic moduli (three Young's moduli, $E_{11} < E_{22} < E_{33}$ and three shear moduli, $G_{23}$, $G_{31}$, and $G_{12}$) were then derived from the orthotropic stiffness tensor. All the μFE analyses for subvolumes were implemented on a Dell XPS PC workstation (Dell, Inc., Round Rock, TX, USA).

## Statistical analysis

Linear correlations between the μMRI microstructural measurements and the corresponding measurements from gold standard μCT images were performed. Linear correlations were also conducted to compare the mechanical measurements of μMR and μCT images including whole bone segment stiffness, trabecular bone stiffness, and six elastic moduli of trabecular bone subvolumes. Paired Student's *t* tests were performed to test for significant differences between corresponding μCT and μMRI measurements.

Furthermore, each of the microstructural measurements based on μMRI and μCT were correlated individually with the mechanical properties derived from the corresponding μCT-based μFE models by linear regression. Next, a forward stepwise multiple linear regression was performed to predict the mechanical properties from the microstructural measurements of μMRI (BV/TV, Tb.N*, Tb.Th*, Tb.Sp*, Tb.N, Tb.Th, Tb.Sp, BS/BV, SMI, Conn.D, and DA) and μCT (BV/TV, Tb.N*, Tb.Th*, Tb.Sp*, BS/

BV, SMI, Conn.D, and DA), respectively. At each step of the forward stepwise regression method, the eligible independent variable with the highest statistical strength ($p < .05$) entered in the model. At any subsequent step where two or more independent variables were selected into the model, the variable with the least statistical strength was removed from the model. The process was terminated when no eligible independent variable exceeded the critical value ($p < .05$) for model entry or when no independent variable in the model reached the standard ($p > .1$) for variable removal. The significant and independent predictors of microstructure parameters were selected to yield the best prediction of each calculated mechanical parameter.

The stepwise multiple linear regressions were performed by SPSS 10.0 software (SPSS, Inc., Chicago, IL, USA). All other statistical analyses were performed using KaleidaGraph 3.6 software (Synergy Software, Reading, PA, USA) with $p \leq .05$ considered statistically significant.

## Results

On qualitative inspection of the μMR and registered μCT images, similar trabecular bone patterns and cortical geometry were found; however, subtle local differences existed in both the trabecular and cortical microstructure between μMR and μCT images (Fig. 1). The local difference was more noticeable when comparing the cubic subvolumes.

The mean and SD of the microstructural and mechanical measurements of the μMR and μCT images are presented in Table 1 and 2. Except for the Tb.N*, all the microstructural μMRI measurements were significantly different from the corresponding μCT measurements ($p < .05$; Table 1). The μMRI-derived microstructural measurements BV/TV, Tb.N*, Tb.N, Tb.Sp*, Tb.Sp, SMI, and Ct.Th correlated significantly and highly ($r^2 = 0.67$ to 0.97) with those derived from the μCT images (Fig. 2). Significant but moderate correlations were also found for the Tb.Th, BS/BV, Conn.D, and DA of μMR and μCT images ($r^2 = 0.23$ to 0.51). However, no correlation existed between the Tb.Th* of μMRI and μCT. Comparing the 3D and 2D measurements from μMRI, we found that Tb.N* and Tb.Sp* from 3D analysis had higher correlation coefficients ($r^2 = 0.92$ and 0.97) and regression slopes closer to 1 than Tb.N and Tb.Sp from 2D analysis ($r^2 = 0.81$ and 0.86) with the μCT measurements. However, the Tb.Th* from 3D analysis had no correlation, whereas the Tb.Th from 2D analysis showed a significant correlation with μCT measurement.

The whole-bone stiffness and trabecular bone stiffness based on μMRI and estimated by μFE analyses correlated significantly and strongly with their gold standards ($r^2 = 0.86$ and 0.96; Fig. 3). In contrast, the elastic moduli of the μMRI trabecular bone subvolume had significant but only moderate correlations with their gold standards ($r^2 = 0.40$ to 0.58; Fig. 3). There was no statistical difference between the trabecular bone stiffness values derived from μMR and μCT images. However, the estimated whole bone stiffness derived from the μMR images was significantly lower than that obtained from the μCT images. In contrast, the estimated elastic moduli of the trabecular bone subvolumes of the μMR images were significantly higher than those obtained from the μCT images.

The trabecular microstructural measurements BV/TV, Tb.Sp*, and SMI of the μCT images and the BV/TV, Tb.N, Tb.Sp*, Tb.Sp, and SMI of the μMRI images were significantly correlated with the whole bone stiffness, trabecular bone stiffness, and elastic moduli of distal tibias estimated by μCT-based μFE analyses (Table 3). Results for Ct.Th from both μMRI and μCT show that it only contributes to whole bone stiffness measurements (Table 3). The Tb.N* values of both the μMR and the μCT images were significantly correlated with most mechanical measurements except that there was no correlation between the Tb.N* of the μCT images and whole bone stiffness. Plate model–based Tb.Th of μMRI was significantly correlated with the whole bone and trabecular bone stiffness but not trabecular bone elastic moduli. Model-independent Tb.Th* estimated from μMRI had no correlation with any of the mechanical measurements, whereas the Tb.Th* estimated from the μCT images was significantly correlated with all the mechanical measurements. The BS/BV of

**Table 1.** Microstructural and Mechanical Measurements of μMR and μCT Images of Distal Tibiae

| μMRI | | | μCT | | | Difference between μMRI and μCT | |
|---|---|---|---|---|---|---|---|
| Parameters | Mean | SD | Parameters | Mean | SD | Mean | SD |
| BV/TV | 0.21 | 0.04 | BV/TV | 0.14 | 0.05 | 0.06 | 0.02 |
| Tb.N* (1/mm) | 1.19 | 0.16 | Tb.N* (1/mm) | 1.18 | 0.18 | 0.01 | 0.05 |
| Tb.N (1/mm) | 1.09 | 0.17 | | | | −0.09 | 0.07 |
| Tb.Th* (mm) | 0.25 | 0.02 | Tb.Th* (mm) | 0.15 | 0.02 | 0.09 | 0.02 |
| Tb.Th (mm) | 0.19 | 0.02 | | | | 0.04 | 0.02 |
| Tb.Sp* (mm) | 0.77 | 0.13 | Tb.Sp* (mm) | 0.83 | 0.13 | −0.06 | 0.02 |
| Tb.Sp (mm) | 0.75 | 0.16 | | | | −0.08 | 0.06 |
| Ct.Th (mm) | 0.66 | 0.15 | Ct.Th (mm) | 0.51 | 0.20 | 0.17 | 0.12 |
| BS/BV (1/mm) | 10.74 | 0.94 | BS/BV (1/mm) | 17.3 | 2.7 | −6.55 | 2.34 |
| SMI | 1.77 | 0.36 | SMI | 1.24 | 0.45 | 0.54 | 0.25 |
| DA | 1.72 | 0.13 | DA | 2.17 | 0.15 | −0.46 | 0.12 |
| Conn.D (1/mm$^3$) | 1.87 | 0.58 | Conn.D (1/mm$^3$) | 4.14 | 1.40 | −2.27 | 1.06 |

**Table 2.** Mechanical Measurements of μMR and μCT Images of Distal Tibias

| | μMRI | | μCT | | Difference between μMRI and μCT | |
|---|---|---|---|---|---|---|
| Parameter | Mean | SD | Mean | SD | Mean | SD |
| Whole bone stiffness (N/mm) | 318,544 | 164,894 | 356,742 | 200,318 | −38,198 | 49,871 |
| Trabecular bone stiffness (N/mm) | 106,195 | 80,784 | 103,107 | 83,752 | 3,088 | 32,166 |
| $E_{11}$ (MPa) | 424 | 157 | 186 | 129 | 238 | 103 |
| $E_{22}$ (MPa) | 766 | 251 | 347 | 170 | 419 | 193 |
| $E_{33}$ (MPa) | 1529 | 439 | 1091 | 500 | 438 | 353 |
| $G_{23}$ (MPa) | 421 | 127 | 228 | 112 | 192 | 104 |
| $G_{31}$ (MPa) | 263 | 86 | 133 | 90 | 130 | 62 |
| $G_{12}$ (MPa) | 211 | 60 | 91 | 53 | 120 | 48 |

μMRI was negatively and significantly correlated with the whole bone stiffness and trabecular bone stiffness, whereas the BS/BV of the μCT images was negatively and significantly correlated with all the mechanical measurements. Except for a weak correlation between the DA of the μMR images and whole bone stiffness, neither μMRI- nor μCT-based DA was correlated with any of the mechanical measurements. The Conn.D of the μMRI images was significantly correlated with trabecular bone stiffness and elastic moduli, whereas the Conn.D measurement of μCT had no correlation with any mechanical measurements except for the trabecular elastic modulus $E_{33}$ (Table 3).

The results from the multiple linear regression analyses suggested that the BV/TV based on μMRI and the BV/TV, Conn.D, and BS/BV based on μCT were the most important predictors of trabecular bone stiffness (Table 4). By adding Ct.Th, the combination of these predictors also provided the strongest

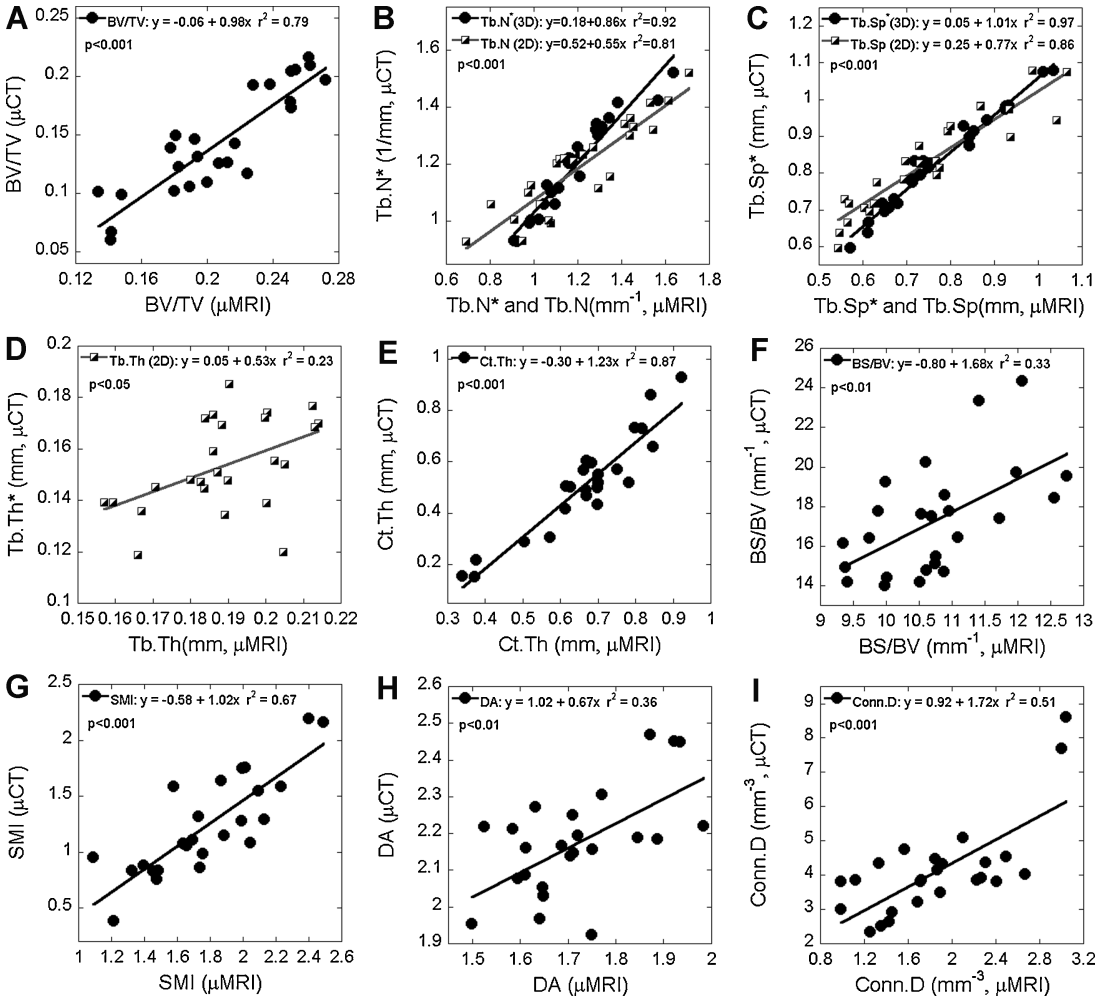


**Fig. 2.** Correlations between microstructural measurements based on μMRI and their respective μCT gold standards.

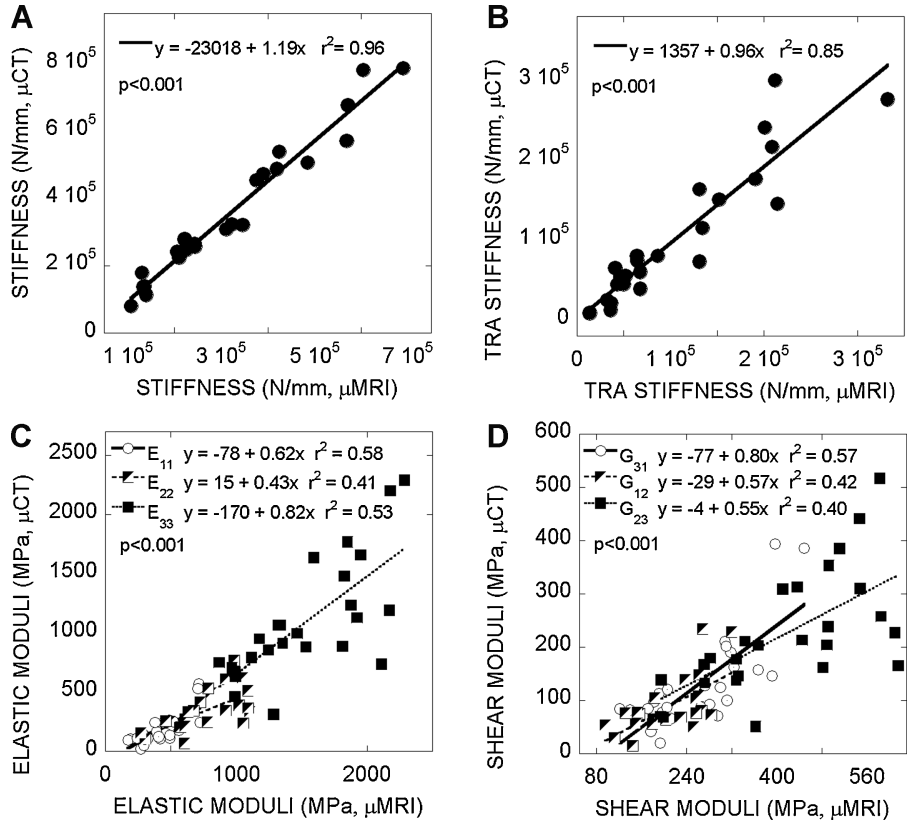


**Fig. 3.** Correlations between (*A*) whole bone stiffness, (*B*) trabecular bone stiffness, (*C*) elastic moduli, and (*D*) shear moduli of registered subvolumes of μMR and μCT images.

prediction for whole bone stiffness. For predictions of $E_{11}$, $E_{22}$, $E_{33}$, $G_{23}$, $G_{31}$, and $G_{12}$ of the trabecular bone subvolumes, BV/TV based on μCT was the only independent and significant predictor. In contrast, the Conn.D based on μMRI was the only independent and significant predictor for $E_{11}$, $G_{31}$, and $G_{12}$, whereas the combination of Conn.D and SMI or DA significantly predicted $E_{22}$, $E_{33}$, and $G_{23}$ of the bone subvolumes (Table 4).

## Discussion

In this study, ex vivo microstructural and mechanical measurements of the human distal tibia from μMR images at a 160-μm isotropic voxel size (subvoxel processed to 53 μm), which are now achievable in vivo, were validated against the gold standard, high-resolution μCT images at a 25-μm isotropic voxel size. Given the large dataset and expensive computational time for whole bone analysis, most published studies have been using smaller subvolumes of trabecular bone for validating μMR with reference to μCT images.[14,26,48,49] To our knowledge, this is the first study that directly compares μMR images of whole bone segments of human distal tibia with μCT images. Moreover, the accuracy of the estimated stiffness of whole bone segments with or without cortex by the μMRI-based FE analyses was addressed for the first time in this study.

Of the microstructural measurements from μMRI, most were correlated significantly with their respective gold standards ($r^2 = 0.33$ to 0.97), with the exception of Tb.Th* ($p > .05$). Particularly high correlations with μCT measurements were found for BV/TV, Tb.N*, Tb.Sp*, Ct.Th, and SMI ($r^2 = 0.67$ to 0.97). These parameters quantify the important microstructural features of both trabecular and cortical bone, and the measurement results based on μMR images could be good indicators of bone quality given their high correlations with the gold standard measurements. On the other hand, greater dispersions were observed in BS/BV, DA, and Conn.D of μMR images compared with gold standard μCT images. BS/BV, DA, and Conn.D are standard measurements for high-resolution μCT images. Correlation results of these measurements suggest that they are more sensitive to the limited image resolution and relatively low SNR of μMR images and thus may not accurately reflect bone quality when applied to μMRI. It should be noted that there is a systematic overestimation of the bone phase: Except for the Tb.N*, the absolute values of the μMRI measurements differed significantly from the gold standard (Table 1). The values of the trabecular BV/TV and Ct.Th of the μMR images were significantly higher and the Tb.Sp was significantly lower than those of the corresponding μCT images. In addition, trabecular bone microstructure represented by μMR images had lower BS/BV, DA, and Conn.D values as well as a higher SMI compared with μCT images, indicating a more rodlike and isotropic trabecular network with less structural connections. These results were comparable with those reported in trabecular bone subvolumes from the radius, calcaneus, and femoral head extracted from μMRI images acquired at 1.5 or 3.0 T.[14,49,57] In general, the correlations of BV/TV, Tb.N*, Tb.Sp*, Tb.N, and Tb.Sp with μCT measurements were similar or slightly higher in this study than those reported previously.[14,49,57]

**Table 3.** Correlation ($r^2$) Between the Microstructural Measurements of μMR and μCT Images and the Mechanical Measurements of μCT Images

| | | μCT-based mechanical properties | | | | | | | |
|---|---|---|---|---|---|---|---|---|---|
| | | Whole bone stiffness | Trabecular bone stiffness | $E_{11}$ | $E_{22}$ | $E_{33}$ | $G_{23}$ | $G_{31}$ | $G_{12}$ |
| μMRI microstructural measurements | BV/TV | 0.44† | 0.54† | 0.37‡ | 0.45† | 0.46† | 0.41† | 0.34‡ | 0.35‡ |
| | Tb.N* (1/mm) | 0.19§ | 0.34‡ | 0.33‡ | 0.36‡ | 0.45† | 0.35‡ | 0.33‡ | 0.36‡ |
| | Tb.Th* (mm) | NS | NS | NS | NS | NS | NS | NS | NS |
| | Tb.Sp* (mm) | (−) 0.24§ | (−) 0.37‡ | (−)0.35‡ | (−) 0.35‡ | (−) 0.45† | (−) 0.34‡ | (−) 0.33‡ | (−) 0.34‡ |
| | Tb.N (1/mm) | 0.27‡ | 0.48† | 0.45† | 0.51† | 0.56† | 0.50† | 0.44† | 0.48† |
| | Tb.Th (mm) | 0.34‡ | 0.49† | NS | NS | NS | NS | NS | NS |
| | Tb.Sp (mm) | (−) 0.32‡ | (−) 0.49† | (−) 0.41† | (−) 0.47† | (−) 0.50† | (−) 0.45† | (−) 0.39† | (−) 0.41† |
| | Ct.Th (mm) | 0.32‡ | NS | NS | NS | NS | NS | NS | NS |
| | BS/BV (1/mm) | (−) 0.37‡ | (−) 0.21§ | NS | NS | NS | NS | NS | NS |
| | SMI | (−) 0.41† | (−) 0.49† | (−) 0.39† | (−) 0.50† | (−) 0.45† | (−) 0.47† | (−) 0.36‡ | (−) 0.39† |
| | DA | 0.16§ | NS | NS | NS | NS | NS | NS | NS |
| | Conn.D (1/mm$^3$) | NS | 0.39† | 0.40† | 0.48† | 0.51† | 0.48† | 0.40† | 0.47† |
| μCT microstructural measurements | BV/TV | 0.35‡ | 0.59† | 0.53† | 0.69 | 0.67† | 0.65† | 0.53† | 0.61† |
| | Tb.N* (1/mm) | NS | 0.23§ | 0.31‡ | 0.36‡ | 0.48† | 0.36‡ | 0.32‡ | 0.36‡ |
| | Tb.Th* (mm) | 0.27‡ | 0.34‡ | 0.26‡ | 0.48† | 0.32‡ | 0.43† | 0.25‡ | 0.33‡ |
| | Tb.Sp* (mm) | (−) 0.23§ | (−) 0.38‡ | (−) 0.38† | (−) 0.40† | (−) 0.50† | (−) 0.38† | (−) 0.37‡ | (−) 0.39† |
| | Ct.Th (mm) | 0.34‡ | NS | NS | NS | NS | NS | NS | NS |
| | BS/BV (1/mm) | (−) 0.29‡ | (−) 0.43† | (−) 0.33‡ | (−) 0.55† | (−) 0.43† | (−) 0.51† | (−) 0.33‡ | (−) 0.42† |
| | SMI | (−) 0.32‡ | (−) 0.56† | (−) 0.47† | (−) 0.64† | (−) 0.57† | (−) 0.63† | (−) 0.47† | (−) 0.54† |
| | DA | NS | NS | NS | NS | NS | NS | NS | NS |
| | Conn.D (1/mm$^3$) | NS | NS | NS | NS | 0.21§ | NS | NS | NS |

*Note:* (–) indicates negative correlation.
†$p < .001$.
‡$p < .01$.
§$p < .05$.
NS: $p > .05$.

**Table 4.** Correlation (Adjusted $r^2$) and Independent Predictors of Multilinear Regression for Prediction of the Gold Standard Mechanical Measurements by the Microstructural Measurements of μMRI and μCT

| μCT-based mechanical properties | μMRI | | | | μCT | | | |
|---|---|---|---|---|---|---|---|---|
| | Independent predictors | Constant | Coefficient | Adjusted $r^2$ | Independent predictors | Constant | Coefficient | Adjusted $r^2$ |
| Whole-bone stiffness | BV/TV | −626,731 | 2,774,470 | 0.60 | BV/TV | −1,501,086 | 6,615,513 | 0.76 |
| | | | | | Ct.Th | | 601,797 | |
| | Ct.Th | | 616,230 | | Conn.D | | −87,140 | |
| | | | | | BS/BV | | 55,260 | |
| Trabecular stiffness | BV/TV | −204,399 | 1,480,246 | 0.52 | BV/TV | −588,734 | 3,225,701 | 0.79 |
| | | | | | Conn.D | | −40,511 | |
| | | | | | BS/BV | | 22,579 | |
| $E_{11}$ | Conn.D | −78 | 141 | 0.38 | BV/TV | −109 | 2,065 | 0.52 |
| $E_{22}$ | SMI | 494 | −207 | 0.55 | BV/TV | −96 | 3,085 | 0.68 |
| | Conn.D | | 118 | | | | | |
| $E_{33}$ | Conn.D | −2088 | 659 | 0.56 | BV/TV | −192 | 9,007 | 0.69 |
| | DA | | 1,136 | | | | | |
| $G_{23}$ | Conn.D | 297 | 82 | 0.53 | BV/TV | −56 | 1,981 | 0.65 |
| | SMI | | −125 | | | | | |
| $G_{31}$ | Conn.D | −51 | 99 | 0.38 | BV/TV | −73 | 1,444 | 0.52 |
| $G_{12}$ | Conn.D | −26 | 62 | 0.45 | BV/TV | −39 | 904 | 0.60 |

*Note:* The order of predictors is the order in which predictors enter the stepwise regression model. All the predictions are statistically significant with $p < .001$.

However, the correlation for the 2D measurement of Tb.Th in this study ($r^2 = 0.23$) was lower than that found in previous studies.[14,49,57] Moreover, the model-independent Tb.Th* showed no correlation with the corresponding μCT measurement, whereas moderate correlations were reported for the radius and calcaneus.[49,57] In this study, the trabecular thickness of the 25 distal tibia specimens ranged from 0.12 to 0.19 mm, as measured by high-resolution μCT images. In contrast, the trabecular thickness derived from μMRI measurement by a distance transformation method was significantly overestimated and fell in a much narrower range (from 0.22 to 0.27 mm). Therefore, the voxel-based distance transformation method used in this study is inadequate for quantifying trabecular thickness in the in vivo μMRI resolution range.

There are several factors that could cause the differences between the measurements of μCT and μMRI. The high resolution and SNR of in vitro μCT result in two distinct phases in the intensity histogram. The bone phase then can be thresholded accurately by using a global thresholding technique.[58] However, at in vivo resolution and SNR, the intensity histogram of μMRI is monomodal. Therefore, there is no unique criterion for the choice of threshold for binarization. Too high a threshold causes artifactual erosion, whereas too low a value leads to inclusion of noise. Here the images were thresholded at an empirically optimized value of 50% BVF to maintain 3D bone microarchitecture with minimal noise.[33] However, the differences in thresholding techniques could cause discrepancies between the measurements of the two modalities. Second, the overestimation of the bone phase could be caused by the partial-volume effect associated with the limited image resolution. This has been shown to be the case in high-resolution peripheral quantitative computed tomography (HR-pQCT), an in vivo CT scanner for bone microstructure at 80-μm voxel size.[59] Third, the larger BV/TV and lower DA values of the μMRI data could be a consequence of artifactual thickening of trabeculae owing to shortened transverse relaxation times ($T_2^*$) of marrow protons in close proximity to bone.[60]

In this study, for both μMR and μCT image-based μFE models, cortical and trabecular bone tissue properties were assumed to be constant and homogeneous for all specimens, and the resulting mechanical measurements of the μFE analysis reflected only the influence of the bone microstructure and not the intrinsic mineral quality. This modeling strategy has been used widely in both μCT- and μMRI-based FE analyses,[2,6,18,61,62] and the μCT-based model has been validated by comparison with mechanical testing results.[63] The significant and high correlations of the estimated whole bone and trabecular bone stiffness of the μMR images with those of the μCT images demonstrate that μMRI-based μFE analyses can directly and accurately quantify whole bone mechanical competence. The linear correlation of trabecular bone stiffness between μMR and μCT images had a 0.96 slope, which was not significantly different from 1. Furthermore, the trabecular stiffness derived from μMRI images was statistically the same as that derived from μCT images. After inclusion of the contribution from the cortex, the correlation of the whole-bone stiffness measurement ($r^2$) between the μMRI and μCT increased from 0.85 to 0.96, although the whole bone stiffness of the μMRI images was slightly underestimated. The partial-volume effect to the mechanical measurements of μMR images was manifest when the analyses were applied to trabecular bone subvolumes. The elastic moduli derived from μMRI images were significantly overestimated and yielded only moderate correlations with the corresponding μCT measurements ($r^2 = 0.40$ to 0.58). The more constrained boundary conditions in these subvolume computations may amplify the overestimation of BV/TV in the μMRI images. At the limited spatial resolution of the μMRI, bone voxels can contain a range of grayscale values resulting from the partial-volume effect. Therefore, a second strategy to generate μFE models is to incorporate the grayscale information of bone voxels by linearly scaling the tissue moduli of the element according to the voxel bone volume fraction.[64] Rajapakse and colleagues previously demonstrated significant and high correlations between the grayscale μFE predictions of μMRI and μCT images at a 160-μm isotropic resolution achievable in vivo based on trabecular bone subvolumes.[64] This modeling strategy should be considered to improve the accuracy of the mechanical measurements from μMR images, especially for analyses of subvolumes of the trabecular bone compartment.

The ability of μMRI-based microstructural measurements to reflect mechanical measurements of the distal tibia is comparable to that of μCT (Table 3). Most of the μMRI-based microstructural measurements were significantly correlated with one or more of the mechanical properties of the distal tibia derived from high-resolution μCT images. However, μMRI-derived Tb.Th* did not correlate with any mechanical measurement. In contrast, Tb.Th* obtained from μCT was significantly correlated with each of the mechanical measurements. Once again, the current spatial resolution of μMRI may not be sufficient for the voxel-based distance transformation method to quantify Tb.Th*.

When all microstructural measurements were combined to predict mechanical competence, the independent predictors appeared to be different for μMR and μCT images. For the μMR images, BV/TV and Ct.Th were the only significant predictors of whole bone stiffness, as well as BV/TV of trabecular bone stiffness. Although many other microstructural measurements were highly correlated with the gold standard measurements or individually contributed to the estimated mechanical properties, they did not make additional contributions to bone stiffness prediction. Furthermore, BV/TV of the μCT images was the only significant predictor of each elastic modulus. In contrast, for μMR images, Conn.D appeared to be an independent and significant predictor of all elastic moduli. The SMI also added independent contributions to $E_{22}$ and $G_{23}$, as well as DA to $E_{33}$. It is interesting that the Conn.D of the μCT images had no contribution to any of the mechanical properties. However, the Conn.D of the μMRI images was shown to be an independent and important indicator of the elastic moduli of trabecular bone.

This study has several limitations. First, μMRI of cadaveric bone is not affected by patient motion artifacts commonly encountered in vivo. Second, all the microstructural analyses in this study were 3D model–independent morphological analyses based on thresholded bone images. These analysis techniques have become the standard for analyzing bone structure of high-resolution μCT images. There was a concern that the spatial

resolution of μMRI images achievable in vivo was lower than that required for the 3D model–independent morphological analyses.[14] However, the data from this study show that most μMRI-derived analyses had significant correlations with μCT reference measurements, except for trabecular thickness (Tb.Th*). An alternative approach is the fuzzy distance transform,[65,66] a technique for measuring structural thickness in the limited-resolution regime. Instead of using the thresholded images, this analysis technique works on the grayscale images, which contain more information about each voxel; therefore, it could provide more accurate estimations of the bone microstructure. The application of this technique to μMR images of the whole trabecular bone segment will be of interest in future studies. Finally, most of the bones used in this study were from male donors. However, in this study, the values of BV/TV by μCT did cover a broad range from 0.06 to 0.22, and μMRI has been shown to be an important imaging modality in clinical studies of both men and women.[7,11,12,16–18]

Currently, high-resolution μMRI is capable of imaging the 3D microstructure of bone but is limited to peripheral skeletal sites. Recent studies have provided in vivo evidence that structural indices derived from μMR images of the radius discriminate between subjects with and without vertebral compression deformities.[7,67] In addition, we recently found significant correlations of the elastic stiffness of the radius and tibia estimated by HR-pQCT images-based μFE models with that of the proximal femur and lumbar spine ($r^2 = 0.4$ to 0.5, $p < .001$) estimated by central quantitative computed tomography (cQCT)–based μFE models in the same subjects.[68] This finding suggests that the mechanical competence of the distal radius and tibia can indicate vertebral and femoral mechanical properties.[68]

In conclusion, the accuracy of microstructural and mechanical measurements of μMR images of the human distal tibia at resolutions achievable in vivo has been tested with reference to the current gold standard, high-resolution μCT. Differences between μMRI and gold standard μCT measurements should be considered when intermodality comparisons are made. However, the high correlations we observed between the microstructural measurements and the mechanical measurements of human distal tibia suggest that μMRI has the potential of becoming a clinical standard for microstructural aspects of bone quality. Microstructural measurements and mechanical parameters of the distal tibia can be derived efficiently from 3D μMRI images and can provide additional information regarding bone fragility.

## Disclosures

FWW is chairman of the Scientific Advisory Board and owns stock in MicroMRI, Inc. All the other authors state that they have no conflicts of interest.

## Acknowledgments

This work was supported in part by grants from the NIH (R01 AR051376, R01 AR055647, T32 EB000814, and F31 EB007448).

## References

1. Sornay-Rendu E, Boutroy S, Munoz F, Delmas PD. Alterations of cortical and trabecular architecture are associated with fractures in postmenopausal women, partially independent of decreased BMD measured by DXA: the OFELY study. J Bone Miner Res. 2007; 22:425–433.
2. Boutroy S, van Rietbergen B, Sornay-Rendu E, Munoz F, Bouxsein ML, Delmas PD. Finite element analyses based on in vivo HR-pQCT images of the distal radius is associated with wrist fracture in postmenopausal women. J Bone Miner Res. 2008;23:392–399.
3. Boutry N, Cortet B, Dubois P, Marchandise X, Cotten A. Trabecular bone structure of the calcaneus: preliminary in vivo MR imaging assessment in men with osteoporosis. Radiology. 2003;227:708–717.
4. Melton LJ 3rd, Riggs BL, Keaveny TM, et al. Structural determinants of vertebral fracture risk. J Bone Miner Res. 2007;22:1885–1892.
5. Melton LJ 3rd, Riggs BL, van Lenthe GH, et al. Contribution of in vivo structural measurements and load/strength ratios to the determination of forearm fracture risk in postmenopausal women. J Bone Miner Res. 2007;22:1442–1448.
6. van Rietbergen B, Majumdar S, Newitt D, MacDonald B. High-resolution MRI and micro-FE for the evaluation of changes in bone mechanical properties during longitudinal clinical trials: application to calcaneal bone in postmenopausal women after one year of idoxifene treatment. Clin Biomech (Bristol, Avon). 2002;17:81–88.
7. Wehrli FW, Gomberg BR, Saha PK, Song HK, Hwang SN, Snyder PJ. Digital topological analysis of in vivo magnetic resonance microimages of trabecular bone reveals structural implications of osteoporosis. J Bone Miner Res. 2001;16:1520–1531.
8. Link TM, Majumdar S, Augat P, et al. In vivo high resolution MRI of the calcaneus: differences in trabecular structure in osteoporosis patients. J Bone Miner Res. 1998;13:1175–1182.
9. Wehrli FW, Hwang SN, Ma J, Song HK, Ford JC, Haddad JG. Cancellous bone volume and structure in the forearm: noninvasive assessment with MR microimaging and image processing. Radiology. 1998; 206:347–357.
10. Wehrli FW. Structural and functional assessment of trabecular and cortical bone by micro magnetic resonance imaging. J Magn Reson Imaging. 2007;25:390–409.
11. Benito M, Vasilic B, Wehrli FW, et al. Effect of testosterone replacement on trabecular architecture in hypogonadal men. J Bone Miner Res. 2005;20:1785–1791.
12. Benito M, Gomberg B, Wehrli FW, et al. Deterioration of trabecular architecture in hypogonadal men. J Clin Endocrinol Metab. 2003;88: 1497–1502.
13. Pothuaud L, Newitt DC, Lu Y, MacDonald B, Majumdar S. In vivo application of 3D-line skeleton graph analysis (LSGA) technique with high-resolution magnetic resonance imaging of trabecular bone structure. Osteoporos Int. 2004;15:411–419.
14. Phan CM, Matsuura M, Bauer JS, et al. Trabecular bone structure of the calcaneus: comparison of MR imaging at 3.0 and 1.5 T with micro-CT as the standard of reference. Radiology. 2006;239:488–496.
15. Link TM, Saborowski O, Kisters K, Kempkes M, et al. Changes in calcaneal trabecular bone structure assessed with high-resolution MR imaging in patients with kidney transplantation. Osteoporos Int. 2002; 13: 119–129.
16. Kazakia GJ, Hyun B, Burghardt AJ, et al. In vivo determination of bone structure in postmenopausal women: a comparison of HR-pQCT and high-field MR imaging. J Bone Miner Res. 2008;23:463–474.
17. Wehrli FW, Ladinsky GA, Jones C, et al. In vivo magnetic resonance detects rapid remodeling changes in the topology of the trabecular bone network after menopause and the protective effect of estradiol. J Bone Miner Res. 2008;23:730–740.

18. Zhang XH, Liu XS, Vasilic B, et al. In vivo μMRI based finite element and morphological analyses of tibial trabecular bone in eugonadal and hypogonadal men before and after testosterone treatment. J Bone Miner Res. 2008;23:1426–1434.
19. van Rietbergen B, Majumdar S, Pistoia W, et al. Assessment of cancellous bone mechanical properties from micro-FE models based on micro-CT, pQCT and MR images. Technol Health Care. 1998;6:413–420.
20. Majumdar S, Newitt D, Mathur A, et al. Magnetic resonance imaging of trabecular bone structure in the distal radius: relationship with X-ray tomographic microscopy and biomechanics. Osteoporos Int. 1996;6:376–385.
21. Lin JC, Amling M, Newitt DC, et al. Heterogeneity of trabecular bone structure in the calcaneus using magnetic resonance imaging. Osteoporos Int. 1998;8:16–24.
22. Krug R, Banerjee S, Han ET, Newitt DC, Link TM, Majumdar S. Feasibility of in vivo structural analysis of high-resolution magnetic resonance images of the proximal femur. Osteoporos Int. 2005;16: 1307–1314.
23. Majumdar S, Genant HK, Grampp S, et al. Correlation of trabecular bone structure with age, bone mineral density, and osteoporotic status: in vivo studies in the distal radius using high resolution magnetic resonance imaging. J Bone Miner Res. 1997;12:111–118.
24. Patel PV, Eckstein F, Carballido-Gamio J, et al. Fuzzy logic structure analysis of trabecular bone of the calcaneus to estimate proximal femur fracture load and discriminate subjects with and without vertebral fractures using high-resolution magnetic resonance imaging at 1.5 T and 3 T. Calcif Tissue Int. 2007;81:294–304.
25. Bauer JS, Monetti R, Krug R, et al. Advances of 3T MR imaging in visualizing trabecular bone structure of the calcaneus are partially SNR-independent: analysis using simulated noise in relation to micro-CT, 1.5T MRI, and biomechanical strength. J Magn Reson Imaging. 2009;29:132–140.
26. Krug R, Carballido-Gamio J, Burghardt AJ, et al. Assessment of trabecular bone structure comparing magnetic resonance imaging at 3 Tesla with high-resolution peripheral quantitative computed tomography ex vivo and in vivo. Osteoporos Int. 2008;19:653–661.
27. Vieth V, Link TM, Lotter A, et al. Does the trabecular bone structure depicted by high-resolution MRI of the calcaneus reflect the true bone structure? Invest Radiol. 2001;36:210–217.
28. Rajapakse CS, Magland J, Zhang XH, et al. Implications of noise and resolution on mechanical properties of trabecular bone estimated by image-based finite-element analysis. J Orthop Res. 2009;27:1263–1271.
29. Chung HW, Wehrli FW, Williams JL, Wehrli SL. Three-dimensional nuclear magnetic resonance microimaging of trabecular bone. J Bone Miner Res. 1995;10:1452–1461.
30. Song HK, Wehrli FW. In vivo micro-imaging using alternating navigator echoes with applications to cancellous bone structural analysis. Magn Reson Med. 1999;41:947–953.
31. Magland JF, Wald MJ, Wehrli FW. Spin-echo micro-MRI of trabecular bone using improved 3D fast large-angle spin-echo (FLASE). Magn Reson Med. 2009;61:1114–1121.
32. Vasilic B, Wehrli FW. A novel local thresholding algorithm for trabecular bone volume fraction mapping in the limited spatial resolution regime of in vivo MRI. IEEE Trans Med Imaging. 2005;24:1574–1585.
33. Magland JF, Wehrli FW. Trabecular bone structure analysis in the limited spatial resolution regime of in vivo MRI. Acad Radiol. 2008; 15:1482–1493.
34. Viola P, Wells WM III. Alignment by maximization of mutual information. Int J Comput Vis. 1997;24:137–154.
35. Collignon A, Maes F, Delaere D, Vandermeulen D, Suetens P, Marchal G. Automated multi-modality image registration based on information theory. In: Bizais Y, Barillot C, di Paola R, eds. Information Processing in Medical Imaging. Dordrecht, The Netherlands: Kluwer Academic Publishers; 1995: pp. 263–274.
36. Ibanez L, Schroeder W, Ng L, Cates J. The ITK Software Guide, 2nd Ed. 2005. Available at http://www.itk.org/ItkSoftwareGuide.pdf. Accessed December 5, 2008.
37. Lu Y, Lau C, Ng L, et al. FusionViewer: an open source toolkit for viewing multimodality images. 2007. Available at http://hdl.handle.net/1926/1331 Accessed December 5, 2008.
38. Hildebrand T, Ruegsegger P. A new method for the model-independent assessment of thickness in three-dimensional images. J Microsc. 1997;185:67–75.
39. Muller R, Hildebrand T, Ruegsegger P. Non-invasive bone biopsy: a new method to analyse and display the three-dimensional structure of trabecular bone. Phys Med Biol. 1994;39:145–164.
40. Ding M, Hvid I. Quantification of age-related changes in the structure model type and trabecular thickness of human tibial cancellous bone. Bone. 2000;26:291–295.
41. Hildebrand T, Laib A, Muller R, Dequeker J, Ruegsegger P. Direct three-dimensional morphometric analysis of human cancellous bone: microstructural data from spine, femur, iliac crest, and calcaneus. J Bone Miner Res. 1999;14:1167–1174.
42. Laib A, Newitt DC, Lu Y, Majumdar S. New model-independent measures of trabecular bone structure applied to in vivo high-resolution MR images. Osteoporos Int. 2002;13:130–136.
43. Hildebrand T, Ruegsegger P. Quantification of bone microarchitecture with the structure model index. Comput Methods Biomech Biomed Engin. 1997;1:15–23.
44. Feldkamp LA, Goldstein SA, Parfitt AM, Jesion G, Kleerekoper M. The direct examination of three-dimensional bone architecture in vitro by computed tomography. J Bone Miner Res. 1989;4: 3–11.
45. Odgaard A, Gundersen HJ. Quantification of connectivity in cancellous bone, with special emphasis on 3-D reconstructions. Bone. 1993; 14:173–182.
46. Cowin SC. Wolff's law of trabecular architecture at remodeling equilibrium. J Biomech Eng. 1986;108:83–88.
47. Odgaard A. Quantification of cancellous bone architecture. In: Cowin SC, ed. Bone Mechanics Handbook, 2nd ed. Boca Raton, Florida, USA: CRC Press LLC; 2001: pp. I4.1–I4.19.
48. Newitt DC, Majumdar S, van Rietbergen B, et al. In vivo assessment of architecture and micro-finite element analysis derived indices of mechanical properties of trabecular bone in the radius. Osteoporos Int. 2002;13:6–17.
49. Sell CA, Masi JN, Burghardt A, Newitt D, Link TM, Majumdar S. Quantification of trabecular bone structure using magnetic resonance imaging at 3 Tesla--calibration studies using microcomputed tomography as a standard of reference. Calcif Tissue Int. 2005;76: 355–364.
50. Van Rietbergen B, Odgaard A, Kabel J, Huiskes R. Direct mechanics assessment of elastic symmetries and properties of trabecular bone architecture. J Biomech. 1996;29:1653–1657.
51. Guo XE, Goldstein SA. Is trabecular bone tissue different from cortical bone tissue? Forma. 1997;12:185–196.
52. Adams MF, Bayraktar HH, Keaveny TM, Papadopoulos P. Ultrascalable implicit finite element analysis in solid mechanics with over a half a billion degrees of freedom. ACM/IEEE Proceedings of SC2004: High Performance Networking and Computing. Pittsburgh, PA, USA; 2004.
53. Adams MF. Evaluation of three unstructured multigrid methods on 3D finite element problems in solid mechanics. Int J Num Meth Eng. 2002;44:519–534.
54. Balay S, Buschelman K, Eijkhout V, et al. PETSc Users Manual. ANL-95/11 - Revision 2.3.3. 2007. Available at http://www-unix.mcs.anl.gov/

petsc/petsc-as/snapshots/petsc-current/docs/manual.pdf. Accessed December 5, 2008.

55. Hollister SJ, Brennan JM, Kikuchi N. A homogenization sampling procedure for calculating trabecular bone effective stiffness and tissue level stress. J Biomech. 1994;27:433–444.
56. Press WH, Teukolsky SA, Vetterling WT, Flannery BP. Numerical Recipes in Fortran, 2nd ed. Cambridge: Cambridge Univ. Press; 1992.
57. Laib A, Beuf O, Issever A, Newitt DC, Majumdar S. Direct measures of trabecular bone architecture from MR images. Adv Exp Med Biol. 2001;496:37–46.
58. Kim CH, Zhang H, Mikhail G, et al. Effects of thresholding techniques on microCT-based finite element models of trabecular bone. J Biomech Eng. 2007;129:481–486.
59. Liu XS, Zhang XH, Sekhon KK, et al. High-resolution peripheral quantitative computed tomography can assess microstructural and mechanical properties of human distal tibial bone. J Bone Miner Res. 2010;25:746–756.
60. Majumdar S, Genant HK. In vivo relationship between marrow $T2^*$ and trabecular bone density determined with a chemical shift-selective asymmetric spin-echo sequence. J Magn Reson Imaging. 1992;2:209–219.
61. Cohen A, Liu XS, McMahon DJ, et al. Bone Microarchitecture and Stiffness in Premenopausal Women With Idiopathic Osteoporosis. J Clin Endocrinol Metab. 2009;94:4351–4360.
62. Liu XS, Sajda P, Saha PK, Wehrli FW, Guo XE. Quantification of the roles of trabecular microarchitecture and trabecular type in determining the elastic modulus of human trabecular bone. J Bone Miner Res. 2006;21:1608–1617.
63. Kabel J, van Rietbergen B, Dalstra M, Odgaard A, Huiskes R. The role of an effective isotropic tissue modulus in the elastic properties of cancellous bone. J Biomech. 1999;32:673–680.
64. Rajapakse CS, Magland JF, Wald MJ, et al. Computational Biomechanics and Structure of the Distal Tibia from High-Resolution MRI and Micro-CT. Bone. 2010 (doi: 10.1016/j.bone.2010.05.0390).
65. Saha PK, Wehrli FW. Measurement of trabecular bone thickness in the limited resolution regime of in vivo MRI by fuzzy distance transform. IEEE Trans Med Imaging. 2004;23:53–62.
66. Saha PK, Wehrli FW, Gomberg B. Fuzzy distance transform: theory, algorithms, and applications. Comput Vis Image Underst. 2002;86:171–190.
67. Ladinsky GA, Vasilic B, Popescu AM, et al. Trabecular structure quantified with the MRI-based virtual bone biopsy in postmenopausal women contributes to vertebral deformity burden independent of areal vertebral BMD. J Bone Miner Res. 2008;23:64–74.
68. Liu XS, Cohen A, Shane E, et al. Bone density, geometry, microstructure and stiffness: relationships between peripheral and central skeletal sites assessed by DXA, HR-pQCT, and cQCT in premenopausal women. J Bone Miner Res. 2010 (doi: 10.1002/jbmr.111).